High-temperature vacancy-induced magnetism in nanostructured materials

D. H. Mosca,[1] J. Varalda,[1] and C. A. Dartora[2,*]

[1]*Physics Department, Federal University of Paraná (UFPR), 81531-980, Curitiba, Paraná, Brazil*

[2]*Electrical Engineering Department, Federal University of Paraná (UFPR), 81531-980, Curitiba, Paraná, Brazil*

(Received 7 June 2023; revised 2 August 2023; accepted 11 September 2023; published 9 October 2023)

Recently, vacancy-induced ferromagnetism in nanostructured materials, that in the pristine state are diamagnetic, aroused great interest among researchers due to their strong potential for the development of new technologies. In particular, vacancy-induced ferromagnetism is persistent at high temperatures, when migration of defect centers by thermal activation becomes non-negligible. For this class of materials, we developed a new and simple phenomenological model with minimal parametrization that describes very well the temperature dependence of the available experimental data. The model assumes the existence of interactions between the effective spins at vacant sites, which becomes responsible for long-range magnetic ordering. On the other side, vacancy migration produces the weakening of the exchange coupling. Our model uses a simple parametrization and very low computational resources, making this approach attractive for applications in science and technology.

DOI: 10.1103/PhysRevB.108.134410

I. INTRODUCTION

In recent decades, several studies have shown that the presence of natural or artificially induced point defects in pristine nonmagnetic nanomaterials can give rise to persistent ferromagnetism even above room temperature [1]. Among the unconventional ferromagnetic materials there are carbon-based materials (carbon nanotubes, fullerenes, microporous and nanofoam carbon) [2–5]; two-dimensional van der Waals materials (like MoS_2, graphene) [6]; freestanding two-dimensional (2D) non–van der Waals crystals (like Cr_2Te_3, h-BN) [7]; and pristine nonmagnetic metal oxides (like ZnO, TiO_2, CeO_2 and so on) [8,9]. Remarkably, a ferromagnetic ground state can emerge in these nanomaterials, even when point defect concentration is below the percolation limit of the lattice structure.

Currently, the role of point defects in unconventional magnetism in nanostructured systems is quite consensual, even though the signal from nanostructures rarely exceeds 10^{-5} emu, which requires attention to the effects of possible unintentional doping [10]. In fact, nonconventional ferromagnetism appears as a universal feature in nanostructured metal oxides [9], and dimensionality reduction apparently does not disturb the robust stability of the magnetic ordering even above room temperature [11–14]. For instance, in undoped oxides a simplification is the absence of magnetic ions as dopants, which are not efficient to improve the magnetic behavior [10]. Vacancy-induced ferromagnetism in the absence of magnetic ion doping is not exclusive to oxides, and it is also present in molybdenum disulfide, being attributed to sulfur vacancies [15].

In the vicinity of a vacant atom in a crystal where valence electrons can be released or removed, the lattice becomes distorted. When the defective centers are donors or acceptors, *n*-type or *p*-type conductivity can occur, but this can be inhibited by charge compensation mechanisms. Furthermore, defect states can be formed within the forbidden energy band, and shifts to the valence or conduction band can occur depending on the specific location and compensation mechanisms. Whatever is the type (cationic or anionic) of vacancy, the charge distribution in its vicinity can result in significant magnetic moments. Core and interstitial magnetic moments are formed due to the spin polarization of the charge distribution resulting from localization and hybridization in the electronic structure. The formation of interstitial magnetic moments favor the interconnectivity between defect centers and long-range magnetic order, even when the concentration of defects is below the percolation limit of the crystalline structure.

Also, a common feature in many materials is the formation of vacancy dimers and complex defect sites that can be oriented preferentially along certain crystallographic axes. As a rule, the concentration of defects and the deformations of the crystal lattice are determinant to define formation energies, migration energy barriers, and anisotropic paths for jumps and rearrangements under thermal activation. Nevertheless, the concentration of native vacancies in oxides are quite dependent on the growth conditions of the nanostructured samples, and it is also dependent on the post-treatment and defect engineering procedures such as ion irradiations [16–19]. Defect engineering can strongly create and modify the concentration of vacancies in nanostructured oxides [16–19] and sulfides [20,21]. Notably, the migrations can be induced without simultaneously producing vacancies at a significant rate, and temperature can has very little effect on the migration rates when electrons are involved [21].

*dartora@ufpr.br

The atom and vacancy migrations along preferable paths in a crystal lattice can be computationally treated by density functional theory (DFT)–based molecular dynamics (MD) methods using empirical pseudopotentials. In DFT-based MD, the local lattice distortions are mainly due to vacant sites, but valence charges of reduced ions also create additional Coulomb interactions. In metal oxides encompassing reduced cations around an oxygen vacancy (VO), these Coulomb potentials often involve electron localization and ion-vacancy complex interactions. Additionally, the oxygen in atomic or ionic forms can also migrate in the volume and often from the volume towards the surface. The relaxation mechanisms lead to a rearrangement of the VO configuration, in which thermally activated enhancement can occur even close to room temperature. As a consequence, a lower concentration of VO may occur in the bulk due to migration and accumulation of VO on the surface [22]. As a rule, the cation migration also occurs preferentially towards the surface and subsurface of the nanostructures. The main reason for this is because closer to the surface, the Coulombic repulsion can be more easily relaxed in the outer layers of the lattice. In this case the reoxidation of the reduced cations can also occur more easily due to exposure to oxygen that also migrates or the supply of oxygen from the external environment, even if not necessarily from the ambient air. Thus the charged ion and vacancy migrations are both responsible for vacancy-induced lattice distortions, and they play an important role in the stabilization of vacancy configuration. At low vacancy concentration, the vacancy formation energy and migration activation energy can be strongly dependent on local strain. Also, the stability of vacancy at isolated surface and subsurfaces relative to bulk oxide is also strain dependent [23,24]. In general, the VO formation energy for several metal oxides decreases with tensile strain according to DFT calculations, with about a 30–100 meV per percent strain decrease with biaxial strain for those systems which showed a decrease in vacancy formation energy [25]. At high vacancy concentration, the configuration of vacancies varies depending on whether the local stress is tensile or compressive. Often, vacancies with no vacant neighboring sites in the first coordination sphere prefer to form dimers under high compressive stress. In general, vacancy-vacancy interactions are determined by the local distortions in the lattice around them together with electrostatic interactions arising from charge redistribution via the long-range Coulombian force. The magnetic interaction due to the local spin must also be considered, and the possibility of spin creation or annihilation (for example, oxygen migration that can create or annihilate empty oxygen sites) may also contribute to the interaction between vacancies.

Despite the success and versatility of the DFT framework, there are two main difficulties. First, is the overestimation of the critical transition temperature from ferromagnetism to paramagnetism in the ferromagnetic ground state of materials, which is a well-known chronic deficiency even in metals [26]. The second refers to the complexity and high computational time consumption to perform a detailed treatment of problems involving molecular dynamics (MD). An alternative approach is to consider the magnetic moments at the centers of polaronic-type defects [27–31]. The polaronic model was originally introduced to describe dilute magnetic oxides and was quickly extended to doped insulating oxides. However, it is not completely satisfactory in systems without charge carriers to mediate magnetic interactions. An extended polaronic model can be applied to unconventional ferromagnetism observed in nanostructures, but the essential ingredient of atom and vacancy migrations at the high-temperature limit is not considered in this model. Recently, a combined approach with standard DFT treatment and a phenomenological model was used to describe the high-temperature ferromagnetism in undoped oxygen-defective cerium dioxide (CeO_2) nanocrystalline films [32]. Essentially, the magnetic moment from VO and localized f electrons calculated by the DFT method were used as input values for the phenomenological model of oxygen and oxygen vacancy migrations along preferred crystallographic directions that provide bridges to long-range magnetic ordering.

In the present work, a new phenomenological model with minimal parametrization is developed to describe vacancy-induced ferromagnetism in materials at temperatures high enough so that thermally activated mechanisms of migration of atoms and vacancies become significant. It is also assumed that the charge distribution with a certain spin polarization can generate free magnetic moments to orient with an externally applied magnetic field along any crystallographic axis. To validate the phenomenological model with reliable parameters, available data of undoped and oxygen-deficient TiO_2 and Ga_2O_3 nanostructures with oxygen vacancies and MoS_2 nanosheets containing sulfur vacancies were used. The choice of these three materials results from the existence of theoretical and experimental reports of nonconventional ferromagnetism, in addition to reports of information on vacancy formation energies and migration barriers in the range of temperatures below those at which the materials lose their remanent magnetization or undergo phase transformations. It is important to emphasize that the model presented here is more concerned with the behavior of the magnetic order as a function of temperature for a variety of materials which have in common a deficiency in the density of chalcogen atoms, which are considered to be responsible for the existence of a localized magnetic moments. Due to its generality, the model is immune to fine structural details of these materials.

II. PHENOMENOLOGICAL MODEL

The evidence that oxygen (or more generally the chalcogen, like sulfur) vacancies in nonstoichiometric oxides (or chalcogenides) are responsible for the existence of a net magnetic moment localized around the defective sites is corroborated both from the experimental side as well as through DFT calculations. Therefore the weakening of magnetic coupling between vacant sites, leading to the eventual disappearance of any magnetic order at some critical temperature T_c, may be attributed at least partially to the diffusion of oxygen (chalcogen) atoms through the defective oxide (chalcogenide) structure. The occupation of a vacant site by a diffusing chalcogen atom is analogous to an electron-hole recombination in semiconductors, leading to the local destruction of a magnetic moment.

At least the following ingredients must be included to obtain a minimal phenomenological model: (i) vacancy

migration, which is considered to be equivalent to the oxygen (or chalcogen atom) transport through the material; (ii) the spin-spin interactions between the vacant sites responsible for long-range magnetic ordering; and (iii) the weakening of the exchange coupling when a vacant site is occupied by an oxygen (or chalcogen atom). The minimal Lagrangian density reads as follows:

$$\mathcal{L} = \mathcal{L}_O + \mathcal{L}_M \ , \tag{1}$$

$$\mathcal{L}_e = i\hbar\phi^\dagger \frac{\partial \phi}{\partial t} + \phi^\dagger \frac{\nabla^2}{2m}\phi + E_0 \phi^\dagger \phi \, , \tag{2}$$

$$\begin{aligned}\mathcal{L}_M = &-\frac{J_0}{2}\sum_{\langle ij\rangle}\left(1-\frac{|\phi(x)|^2}{n}\right)\left(1-\frac{|\phi(y)|^2}{n}\right)\\ &\times \delta(x-x_i)\delta(y-y_j)\mathbf{S}_i\cdot\mathbf{S}_j\\ &- g_0\mu_B\sum_i\left(1-\frac{|\phi(x)|^2}{n}\right)\delta(x-x_i)\mathbf{B}_e(x)\cdot\mathbf{S}_i \, ,\end{aligned} \tag{3}$$

where ϕ is the oxygen (or chalcogen atom) field, such that $|\phi(x)|^2$ is the density of ions diffusing through the material at the space-time position $x = (\mathbf{x}, t)$, E_0 is an effective activation energy, which includes averaged Coulomb interactions, m is the atomic mass of oxygen (or another chalcogen atom), g is an effective gyromagnetic factor for the vacancies, $\mu_B = 9.27 \times 10^{-24}\,\mathrm{A\,m^2}$ is the Bohr magneton, J_0 denotes the effective exchange integral for neighboring vacancies, $\langle ij\rangle$ refers to the summation over first neighbors only, n is an averaged crystalline density in d spatial dimensions, and $\mathbf{B}_e$ is the applied magnetic field. The generating functional for calculating the relevant physical quantities can be expressed in terms of a path integral [33] as follows:

$$\mathcal{Z}[\mathbf{B}_e] = \int \mathcal{D}\mathbf{S}\int \mathcal{D}(\phi,\phi^\dagger)\rho(\mathbf{S})e^{\frac{i}{\hbar}\int d^{d+1}x\,\mathcal{L}(\mathbf{S},\phi,\phi^\dagger)} \, , \tag{4}$$

where $\mathcal{D}(\mathbf{S})$ and $\mathcal{D}(\phi,\psi^\dagger)$ are functional integration measures related to the local spins and the oxygen field, respectively, $\rho(\mathbf{S})$ is the spin statistical distribution, and d is the number of spatial dimensions. After the functional integration of the ϕ and going to the imaginary time $t = -i\hbar\beta$ representation, where $\beta = (k_B T)^{-1}$ is the reciprocal of the absolute temperature T and k_B is the Boltzmann constant, the lowest order approximate partition function $\mathcal{Z}[\mathbf{B}_e]$ can be written as follows:

$$\mathcal{Z}[\mathbf{B}_e] = \int \mathcal{D}\mathbf{S}\rho(\mathbf{S})e^{-\beta\int d^d\mathbf{x}\int d^d\mathbf{y}\,\mathcal{H}_{eff}(\mathbf{S})} \, , \tag{5}$$

apart from irrelevant normalization constant, and $\mathcal{H}_{eff}(\mathbf{S})$ is now the effective Hamiltonian density given by

$$\begin{aligned}\mathcal{H}_{eff} = &-\frac{J(T)}{2}\sum_{\langle ij\rangle}\delta(\mathbf{x}-\mathbf{x}_i)\delta(\mathbf{y}-\mathbf{y}_j)\mathbf{S}_i\cdot\mathbf{S}_j\\ &- g(T)\mu_B\sum_i\delta(\mathbf{x}-\mathbf{x}_i)\mathbf{B}_e(\mathbf{x})\cdot\mathbf{S}_i \, ,\end{aligned} \tag{6}$$

where the spin couplings become temperature dependent:

$$J(T) = J_0\left[1-\frac{2A}{n}\left(\frac{T}{T_c}\right)^{d/2}e^{-\beta E_0}\right], \tag{7}$$

$$g(T) = g_0\left[1-\frac{A}{n}\left(\frac{T}{T_c}\right)^{d/2}e^{-\beta E_0}\right], \tag{8}$$

being $A = (2\pi m k_B T_c/\hbar^2)^{d/2}$. At this point the Curie temperature T_c is unknown and must be calculated from an effective ferromagnetic problem. Using the Curie-Weiss mean-field strategy, the magnetization $M(T)$ is obtained solving the resulting transcendental equation, which involves the Brillouin function for an effective spin S:

$$\begin{aligned}\frac{M(T)}{M_s} = &\frac{2S+1}{2S}\coth\left[\frac{g(T)(2S+1)\mu_B B_{eff}}{2k_B T}\right]\\ &-\frac{1}{2S}\coth\left[\frac{g(T)\mu_B B_{eff}}{2k_B T}\right],\end{aligned} \tag{9}$$

where the effective magnetic field depends explicitly on the magnetization, being given by

$$B_{eff} = \mu_0 H_e + \frac{zJ(T)M(T)/M_s}{g(T)\mu_B} \, , \tag{10}$$

where μ_0 is the vacuum magnetic permeability, z is the effective coordination number, and $M_S = n_V S g_0 \mu_B$ is the saturation magnetization, which directly depends on the vacancy density n_V and its effective magnetic moment $\mu_{eff} = S g_0 \mu_B$. Spontaneous magnetization is obtained in the limit $H_e \to 0$ by solving Eq. (9) numerically. Here the numerical method employed is pretty simple and involves finding the roots of an equation of the form $M(T)/M_s - B_S[M(T)/M_s] = 0$, where $B_S[M(T)/M_s]$ is the right-hand side of (9).

The magnitude of the exchange parameter J_0 can be estimated using simple arguments. As a matter of fact, the exchange energy comes from a quantum mechanical correction to the Coulomb interaction, depending on the overlap between the wave functions of the identical particles being interchanged. For hydrogenlike orbitals, $\psi(r) \sim e^{-\alpha r}$, and the average distance between two neighboring vacancies depends on the vacancy density n_V as $r \approx n_V^{-1/d}$. This way the exchange energy can be approximated by the following expression:

$$J_0(n_V) \approx \frac{q^2}{4\pi\epsilon} n_V^{1/d}\left(1+\frac{\alpha}{n_V^{1/d}}\right)e^{-\alpha n_V^{-1/d}} \, , \tag{11}$$

where q is the electric charge associated with the vacancy, $\alpha = 1/a_0$ is an effective screening associated with the inverse of the effective Bohr radius a_0 of the atomic or molecular orbitals being considered, staying in the range of $10^9 - 10^{10}\,\mathrm{m^{-1}}$, $\epsilon = \epsilon_r\epsilon_0$ is the dielectric permittivity of the material, $\epsilon_0 = 8.854 \times 10^{-12}\,\mathrm{F/m}$, and ϵ_r is the relative dielectric permittivity of the material.

The Curie temperature T_c can only be obtained by solving a transcendental equation resulting from the analysis of the magnetic susceptibility in the limit $\mu_B B_{eff}/(k_B T) << 1$. It takes the following form:

$$T_c = T_{c0}\left[1-\frac{2A_0}{n}\left(\frac{T_c}{T_{c0}}\right)^{d/2}e^{-E_0/(k_B T_c)}\right], \tag{12}$$

where $T_{c0} = zJ_0(S+1)/(3k_B)$ is the predicted Curie temperature, neglecting the effect of vacancy migrations such that

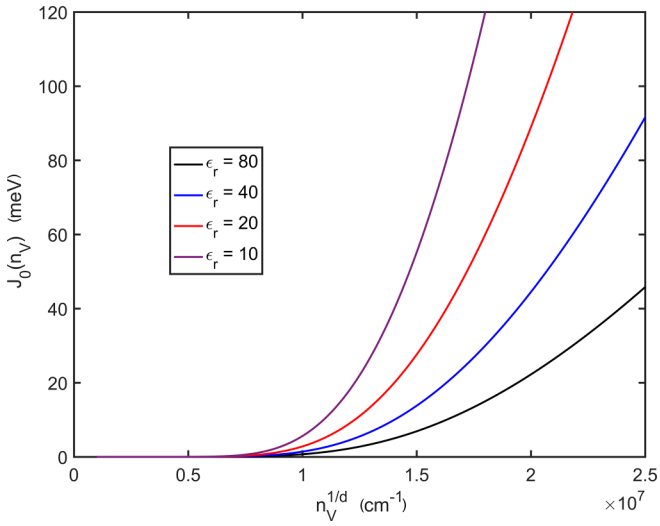

FIG. 1. The exchange energy $J_0(n_V)$ is plotted as a function of $n_V^{1/d}$ for a few values of the relative dielectric permittivity ϵ_r, keeping fixed the values of the vacancy charge $q = +2e$ and the effective parameters $\alpha^{-1} = 150$ pm, $z = 6$, and $S = 1/2$.

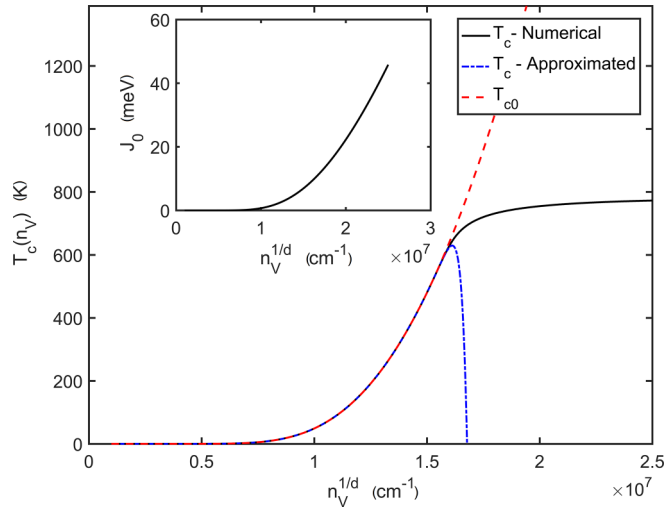

FIG. 2. The Curie temperature $T_c(n_V)$ is plotted against $n_V^{1/d}$, using $n = 5 \times 10^{22}$ cm^{-3}, the dielectric constant $\epsilon_r = 40$, $E_0 = 1$ eV, the vacancy charge $q = +2e$, mass $m = 16$ Da, and the effective parameter $\alpha^{-1} = 150$ pm. The inset displays the exchange parameter J_0 as a function of $n_V^{1/d}$.

$J(T) = J_0$ and $A_0 = (2\pi m k_B T_{c0}/\hbar^2)^{d/2}$. However, a useful approximation is obtained by replacing $T_c = T_{c0}$ in the right-hand side of (12), yielding

$$T_c = T_{c0}\left[1 - \frac{2A_0}{n} e^{-E_0/(k_B T_{c0})}\right]. \tag{13}$$

Notice that this last expression reaches a maximum and then breaks down completely when $\frac{2A_0}{n} e^{-E_0/(k_B T_{c0})} \to 1$, allowing us to estimate in an approximate way a maximum value for T_c. Therefore an analytic approximation for the maximum T_c is given below:

$$T_{c,max} \approx \frac{(2E_0/d)}{k_B \ln\left[\frac{2^{1+2/d}\pi m k_B z(S+1)J_{0,max}}{\hbar^2 n^{2/d}}\right]}, \tag{14}$$

with $J_{0,max}$ the value of the exchange parameter at a critical value of vacancy concentration n_V. Expression (14) permits us to conclude that the higher the barrier E_0 the higher the Curie temperature, as expected, since vacancy migration, which introduces magnetic disorder, becomes unfavorable at high values of E_0. Also, keeping all the other parameters fixed, it is expected that critical temperature is inversely proportional to the effective dimensionality of the system.

For the sake of reference, in Fig. 1 the exchange energy $J_0(n_V)$ given by (11) is plotted as a function of $n_V^{1/d}$ for a few values of the relative dielectric permittivity ϵ_r, keeping fixed the values of the vacancy charge $q = +2e$ (typical in oxides) and the effective parameter $a_0 = \alpha^{-1} = 150$ pm and effective spin $S = 1/2$. The exchange energy scale is set by the factor $q^2/(4\pi\epsilon) \approx 5.75 \times 10^{-7}/\epsilon_r$ eV cm. For $\epsilon_r \sim 40$ and $n_V^{1/d} \sim 2 \times 10^7$ cm^{-1}, the value of J_0 calculated with (11) would be as high as 45 meV. For a typical cubic lattice this would imply a $T_{c0} \sim 1560$ K, which is clearly much larger than typical experimental values. However, T_c will be lowered by migration effects, which are taken into account using Eq. (13). In the present case T_c will approach a more realistic value of 800 K, as can be seen in Fig. 2, which illustrates the behavior of the Curie temperature T_c as a function of $n_V^{1/d}$, for the dielectric constant $\epsilon_r = 40$, $E_0 = 1$ eV, and chalcogen density $n = 5 \times 10^{22}$ cm^{-3} in $d = 3$, while keeping other parameters the same as those used to obtain Fig. 1.

We obtained the Curie temperature as a function of $n_V^{1/d}$ by numerically solving Eq. (12) and compared it to the results obtained from (13) and the uncorrected T_{c0} as well. As a general feature of the present model, at first, T_c increases exponentially with $n_V^{1/d}$, which is expected on the grounds that a higher vacancy concentration produces a decrease in the average distance between the magnetic moments generated by the vacancies, enhancing the exchange energy J_0. However, the effect of chalcogen ion diffusion becomes more probable at higher vacancy concentration and introduces a saturation mechanism for the value of T_c, which does not increase significantly after a critical value of the vacancy density is reached. The critical n_V depends on the activation energy parameter E_0, the effective charge q of the defective site, the dielectric constant ε_r, and the effective radius a_0 of the material. Close to the critical value of n_V the approximated expression (13) for T_c has a maximum which is close to but underestimates the true Curie temperature. Beyond that point the approximation breaks down completely. Nonetheless, the increase of n_V above its critical value in the material produces a proportional augment in the value of the saturation magnetization, $M_s = n_V S g_0 \mu_B$.

It is worth mentioning that in the phenomenological model put forward there are only a few input parameters, viz. migration barrier energy E_0, spin-spin exchange energy J_0 at $T = 0$, vacancy concentration n_V, and effective magnetic moment per vacancy. Compared to the model previously applied to describe the high-temperature magnetization of oxygen-defective CeO_2 [32], the present one is more appropriated to materials with electrons showing stronger hybridization and less localization in the cationic sites.

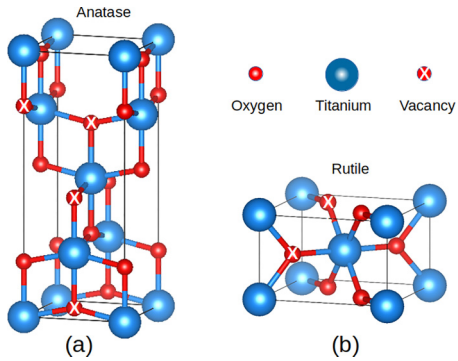

FIG. 3. Two main titanium dioxide polymorphs in which titanium exhibiting octahedral geometry is bonded to six oxide anions. The crystal structures of (a) anatase and (b) rutile have tetragonal symmetry. Different possible locations of oxygen vacancies are shown.

III. RESULTS AND DISCUSSION

In the present section the theoretical results obtained from the proposed model are contrasted to the experimental data for the magnetization versus temperature of nonstoichiometric chalcogenides displaying magnetism, which is assumed to be induced by vacancies. Possible locations and migration paths of isolated vacancies and their complexes in unrelaxed crystalline structures are discussed in model validation.

A. TiO_2

Titanium dioxide (TiO_2 or titania) is a naturally occurring oxide at atmospheric pressure, exhibiting two main polymorphs, rutile and anatase. Rutile (space group $P42/mnm$) and anatase (space group $I4/amd$) both have tetragonal structure. Rutile is the stable phase whereas anatase is metastable. However, nanosized forms of TiO_2 tend to form in the metastable anatase phase due to the lower surface energy of this phase relative to the equilibrium rutile phase [34], because the spatial arrangement of the TiO_6 octahedra into long-range ordered anatase structure tends be less restrictive in relation to rutile. TiO_6 octahedra shares four edges in anatase and two in rutile, as shown in Fig. 3.

Crystalline and highly stoichiometric rutile TiO_2 has high dielectric constant $\epsilon_r = 84 - 100$ [35,36], whereas oxygen-defective TiO_2 samples tend to exhibit slightly lower values of $\epsilon_r = 70$. Anatase TiO_2 structures exhibit values $\epsilon_r = 30 - 40$ [35]. Structurally disordered TiO_2 samples can exhibit values as low as $\epsilon_r = 20$ [37]. The oxygen diffusion in rutile TiO_2 has been investigated extensively by several techniques [38–42] due to its wide range of applications [43,44]. Particularly, the oxygen diffusion is an essential ingredient in the TiO_2 resistive switching, in which the main mechanism is described through the formation of oxygen-deficient fractal filaments induced by electric field bias [45] together with the high mobility of doubly ionized oxygen vacancy (VO^{-2}) [46]. The effective oxygen self-diffusion coefficient is $D \approx 10^{-13}$ cm^2/s for rutile TiO_2 at 750°C [47].

In TiO_2 nanostructures with geometries of nanofiber, nanoribbon, nanotube, and thin film, oxygen and oxygen vacancy migrations, as well as the interaction between these vacancies, are relatively well known along with the transformation temperature from rutile to anatase [48–52]. In particular, while the transformation from anatase to rutile phase occurs above 600°C at 1 atm (101 kPa) pressure, rutile cannot be transformed into anatase [34].

The activation energy barrier values for the VO diffusion in TiO_2 spread from 0.35 to 2.42 eV, whereas the VO diffusion constant is found between $D = 1 \times 10^{-16}$ cm^2/s at 550 K and $D = 5 \times 10^{-15}$ cm^2/s at 800 K [53]. The diffusion length $\sqrt{Dt}$ is experimentally found to be as large as 5 nm under isochronal annealing conditions for $t = 5$ min [54]. DFT calculations result in magnetic moment values that depend strongly on the local lattice relaxation and detail of the theoretical calculations [55,56]. Nevertheless, diffusion timescales exceed the present-day computer technology for quantum chemical MD methods, which only afford a few picoseconds of simulation [57]. As a matter of fact, every VO gives two electrons in the titania conduction band, which can improve the electrical conductivity. The electrons left behind from the released oxygen can become localized, reducing Ti^{4+} to Ti^{3+}, and a redistribution of charges due to Ti3d - O2p hybridization can result in a polarized charge distribution. Rutile TiO_2 with a cation density of about 2.9×10^{22} cm^{-3} [28,58] exhibits room-temperature ferromagnetism, and it is required that at least 1% of this value must reach the threshold concentration in order for the onset of magnetic ordering to be possible [58]. However, room-temperature ferromagnetism is also observed in undoped oxygen-defective TiO_2 nanostructures with much lower VO concentrations. For example, in rutile $TiO_{1.95}$ thin films the room-temperature ferromagnetism is found with $n_V \approx 1.6 \times 10^{21}$ cm^{-3} [56]. In rutile and anatase oxygen-defective TiO_2 nanotubes with diameters between 40 and 160 nm with 3.0×10^{16} cm^{-3} and 60×10^{16} cm^{-3}, respectively [58], room-temperature ferromagnetism is also found. Higher VO concentrations promoted by ion bombardments can induce room-temperature ferromagnetism with enhanced anisotropic magnetization [16].

Therefore it is almost consensual that the presence of VO contributes to spontaneous magnetizations above room temperature in TiO_2, making it a suitable material to put the model presented here to the test. Assuming a typical dielectric constant for anatase TiO_2 in the range of $\epsilon_r \sim 40$, an effective VO charge $q = +2e$, an oxygen density of $n \approx 6.4 \times 10^{22}$ cm^{-3}, and $a_0 \sim 150$ pm for Ti valence orbitals (which are more extended than oxygen and tend to overlap more, making the most relevant contribution for J_0), expression (11) yields $J_0 \sim 25$ meV for $n_V \sim 5 \times 10^{21}$ cm^{-3} in $d = 3$. For an effective moment of $\mu_{eff} \sim 0.5\mu_B$ per VO^{2+}, it leads to a saturation magnetization of $M_s = \mu_{eff} n_V \approx 23$ emu/cm^{-3}. Adopting a typical coordination number $z = 6$ and an activation energy $E_0 = 0.7$ eV, the numerical solution of (12) for $d = 3$ yields for the critical vacancy density $n_V^{1/3} \approx 1.52 \times 10^7$ cm and a maximum Curie temperature $T_c \approx 580$ K. Meanwhile, considering a film of thickness ~1 nm as a two-dimensional system, we obtain for the critical vacancy density $n_V^{1/2} \approx 1.67 \times 10^7$ cm^{-1} and a maximum $T_c \approx 900$ K, which is significantly higher than the bulk value ($d = 3$). Of course, the limits on the maximum attainable T_c are dependent on the precise value of the activation energy E_0 and the dielectric

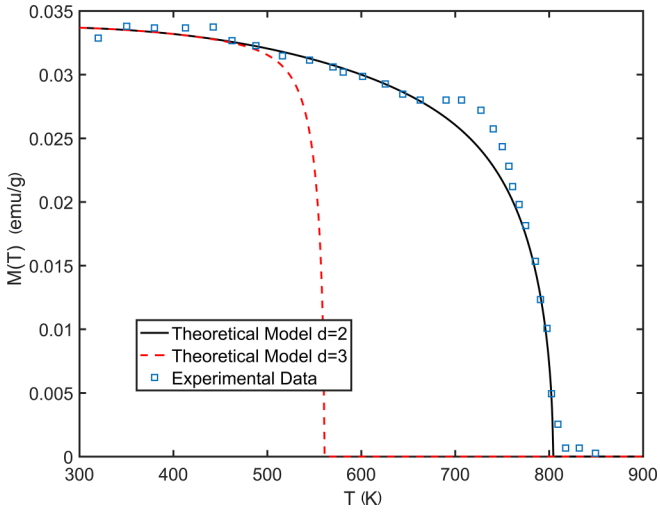

FIG. 4. Comparison between the theoretical model proposed here and the selected experimental data for TiO_2 nanoribbons, taken from Fig. 10 of the paper by Santara *et al.* [59]. The following parameters were used: effective spin $S = 1/2$, effective exchange energy $J_0 = 26$ meV, $z = 6$, oxygen activation energy $E_0 = 0.72$ eV, and oxygen density is taken to be $n = 6.4 \times 10^{22}$ cm^{-3} for $d = 3$ and $n = 6.4 \times 10^{15}$ cm^{-2} for $d = 2$.

constant ϵ_r, which in turn are dependent, among other things, on the structural phase, morphology, and disorder of the fabricated samples.

As a first concrete example consider the solvothermally synthesized undoped TiO_2 nanoribbons reported in Ref. [59]. These nanoribbons in anatase phase display room-temperature ferromagnetism induced by the presence of oxygen vacancies. The comparison between experimental data and theoretical results is displayed in Fig. 4. Based on the amount of experimental data for vacancies in TiO_2, the following parameters were taken as the input for the model: effective vacancy spin $S = 1/2$, coordination number $z = 6$, oxygen density $n = 6.43 \times 10^{15}$ cm^{-2} for $d = 2$ and $n = 6.43 \times 10^{22}$ cm^{-3} for $d = 3$, $\epsilon_r \approx 30$ for anatase, and vacancy density $n_V^{1/d} = 1.64 \times 10^7$ cm^{-1}, which results in $J_0 \approx 27$ meV. The oxygen activation energy E_0 was used to fit the experimental data and good agreement was achieved, setting $E_0 = 0.72$ eV, which is in the range of reported values for VO activation in TiO_2 [53]. The theoretical model was solved in $d = 2$ and $d = 3$. As can be seen, for $d = 2$ the model can be used to predict qualitatively the Curie temperature $T_c \approx 800$ K, in good agreement with experimental data. However, considering $d = 3$ substantially decreases the Curie temperature, contradicting the experimental results. The problem becomes even worse if one considers that the activation energy increases. It can be concluded that the TiO_2 nanoribbons behave more closely to a 2D system, as expected. From the experimental data on the saturation magnetization, $M_s \approx 0.06$ emu/g, we obtain the effective ferromagnetic moment to be $\mu_{eff} = M_s/n_V \approx 0.01\mu_B$, which is two orders of magnitude smaller than $\mu_{eff} \sim 1.0\mu_B$. This can be attributed to a clustering effect of the ferromagnetic regions due to structural and morphological irregularities in the film induced at the growth process. In any case, it is worthy of mention to notice that the exact value of the saturation and the Curie temperature are functions of the VO density, which is set by the film stoichiometric characteristics.

Going further, the model is applied to the oxygen-deficient anatase $TiO_{2-\delta}$ film grown on (1 0 0) $LaAlO_3$ reported in Ref. [60]. Ferromagnetic order was observed up to 880 K in those TiO_2 films, and electrical conductivity combined with magnetization versus temperature measurements almost unequivocally leads to the conclusion that the magnetic ordering is a consequence of localized spins around the defective sites, with spin $S = 1/2$ or $S = 1$ and a spin density around 4×10^{21} cm^{-3}. A noticeable change in the magnetization was observed at ∼350 K. The authors attributed that effect to the coexistence of a ferromagnetic phase with a lower critical temperature, $T_c \sim 600$ K, and ferrimagnetic contribution having a larger critical temperature, ∼880 K. They were able to fit the experimental data using power laws of the form $M(T)/M_S = (1 - T/T_c)^\beta$, where T_c and β have different values, before and after the kink appears. Within the present model a slightly distinct approach is considered to accommodate the experimental data extracted from Ref. [60]. It is supposed that a coexistence of two structural phases exists in the fabricated films, being predominantly in the anatase form. These phases possess distinct magnetic couplings and activation energies for the oxygen migration. This way, the full magnetization of the sample is given by the sum of two contributions, $M(T) = M_1(T) + M_2(T)$, where $M_1(T)$ and $M_2(T)$ are obtained by solving (9) with distinct exchange couplings, $J_1(T)$ and $J_2(T)$. Let us consider an anatase phase $\epsilon_r \approx 30$ and coordination $z = 6$ again, with a density around $n_V^{1/d} \approx 1.25 \times 10^7$ cm^{-1}, superimposed to a more disordered structural phase, which reduces the dielectric constant ($\epsilon_r \approx 20$) and at the same time lowers the coordination number $z = 4$, with $n_V^{1/d} \approx 9.8 \times 10^6$ cm^{-1}. This way, using expressions (11) and (12) to obtain the exchange coupling and Curie temperature, we obtain $J_{01} = 26$ meV and $T_{c1} = 790$ K, $J_{02} = 17$ meV and $T_{c2} = 393$ K, for the anatase and the disordered phase, respectively. Figure 5 shows the fitting of experimental data extracted from Ref. [60] using the proposed theoretical model. For the sake of comparison, the expressions $M_1(T) = M_{S1}(1 - T/600)^{0.34}$ and $M_2(T) = M_{S2}(1 - T/880)^{0.32}$, with $M_{S1} = 48.5$ emu/cm^3 and $M_{S2} = 46.2$ emu/cm^3, are also plotted. The parameters of the model are the following: dimensionality of the system is $d = 2$, spin $S = 1/2$, $zJ_{01} = 156$ meV, $E_{01} = 0.72$ eV, $zJ_{02} = 68$ meV, $E_{02} = 0.4$eV. Taking the experimental value for the saturation magnetization to be 550 G ≈43.8 emu/cm^3 [60], a good agreement between theory and experimental values is obtained using the fractions $f_1 = 0.79$ of the film in the anatase structure and $f_2 = 1 - f_1 = 0.21$ in the other structure. These values lead to $M_{S1} \approx 34.6$ emu/cm^3 and $M_{S2} = 9.2$ emu/cm^3, resulting in $\mu_{eff,1} \approx 2\mu_B$ and $\mu_{eff,2} \approx 1.0\mu_B$. The parameter corresponding to the oxygen density is taken to be $n = 6.43 \times 10^{15}$ cm^{-2} in $d = 2$.

B. Ga_2O_3

Gallium oxide (Ga_2O_3 or gallia) crystallizes in five different phases referred to as $\alpha, \beta, \gamma, \delta$ and ε. The monoclinic β-Ga_2O_3 is the most stable phase, whereas the γ phase is derived from the cation-defective molecular formula AB_2O_4 [61,62], the structure of which has a cubic close packing

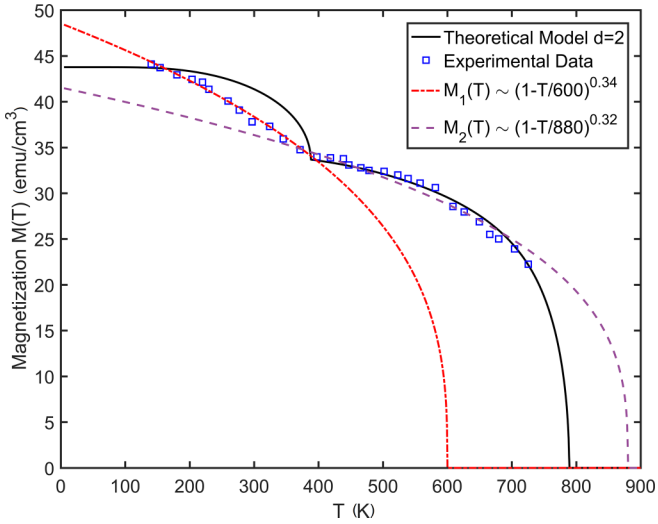

FIG. 5. Comparison between the theoretical model proposed here and the experimental data for oxygen-deficient anatase $TiO_{2-\delta}$ film grown on (1 0 0) $LaAlO_3$, extracted from the Fig. 3 of the paper by Yoon *et al.* [60]. The main parameters used are effective spin $S = 1/2$, effective exchange energies $zJ_{01} = 156$ meV and $zJ_{02} = 68$ meV, and oxygen activation energies $E_{01} = 0.72$ eV and $E_{02} = 0.40$ eV. It is assumed 79% in phase 1 and 21% in phase 2, $d = 2$ and $n = 6.4 \times 10^{15}$ cm^{-2}.

arrangement of oxide ions, with cations (A and B) in some of the interstitial tetrahedral and octahedral voids, respectively. The standardized γ-$Ga_{2.67}O_4$ is commonly represented by a minimal supercell γ-$Ga_{24}O_{32}$ [63] with a cation-defective spinel-like cubic structure (see Fig. 6). This representation contains rutile chains running along ⟨110⟩ directions, and these chains can be viewed as pathways for electrons when a major fraction of the octahedral cation sites are occupied by the heavy p-block cations with s^0 electronic configuration [61].

In oxygen-deficient γ-Ga_2O_{3-x} films ($0.42 < x < 0.60$), the crystalline structure is of the disordered cubic spinel type, where the oxygen atoms are arranged in a cation-deficient compact cubic lattice with the cations randomly occupying tetrahedral and octahedral sites of the lattice. The exothermic

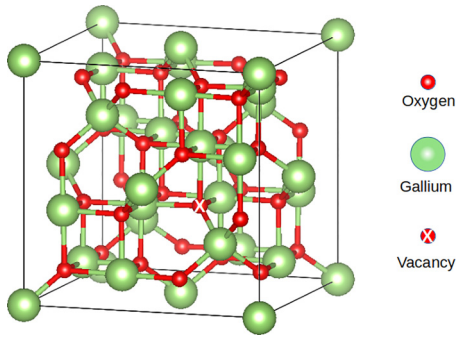

FIG. 6. Optimized γ-Ga_24O_32 unit cell from the standardized crystal structure of the γ phase of gallium oxide (Ga_2O_3). An oxygen vacancy is indicated in the random configuration of Ga^{3+} ions with tetra and octahedral coordinates.

transformation from γ-Ga_2O_3 to monoclinic β-Ga_2O_3 is irreversible above 873 K, but it remains reversible in the range of 650–800 K [64,65]. Studies report unconventional ferromagnetism at room temperature for the γ and β phases, whose formation energies and migration barrier were also studied even under known stress values. Additionally, the transformation from γ to β phase is dependent on VO migration and stress relaxation [66].

As a rule, metastable sites are usually high-symmetry configurations along the migration paths, and this is how the vacancy diffusion activated by increasing temperature improves crystalline properties of γ-Ga_2O_3 towards disordered β-Ga_2O_3 films [67]. The intrinsic disorder in the low-symmetry structure of the Ga_2O_3 allows for a number of possible paths for the migration of oxygen and gallium vacancies (VO and VGa, respectively). The formation energy calculations of several works yield converged results [66,68–72], indicating negative formation energies in vacuum or in an oxygen-poor environment for triple-ionized gallium vacancies (VGa^{3-}) and double-ionized oxygen vacancies (VO^{2+}). Since the lower the formation energy the higher the vacancy concentration in a Ga_2O_3 sample, it is more likely that these two vacancies form in the samples. Despite that VGa^{3-} exhibits significantly lower migration barriers compared to VO^{2-} (using the definition of the migration barrier as the energy difference of the saddle point and the lowest energy state), with the energy barriers for most probable jumps between 0.7 and 2.2 eV for VGa^{3-} and between 1.2 and 2.7 eV for VO^{2+} [66], a simple vacancy VGa^{3-} at the tetrahedral Ga site is unfavorable in β-Ga_2O_3. The main reason is that several mechanisms help VGa^{3-} diffusion mainly along the [001] crystal direction, lowering the overall barrier value. The estimated annealing temperature for VGa^{3-} is about 375 K for the [001] direction and 805 K for the remaining directions [72]. A first-principles study of VGa-induced magnetism in β-Ga_2O_3 [70] reveals that VGa in both sixfold-coordinated octahedral sites and the fourfold-coordinated tetrahedral sites can lead to a spin-polarized ground state. In this case, ferromagnetism can be explained by a molecular orbital model consisting of uncompensated O^{2-} $2p$ dangling bonds. Only the local magnetic moment induced by the single isolated VGa in tetrahedral sites leads to a stable ferromagnetic order at high temperature. For a supercell with 120 atoms, the net magnetic moment is $1.37\mu_B$, the nearest-neighbor exchange parameter J_0 is 55 meV, and the transition temperature T_c is about 964 K [70]. Particularly, ultrathin nanosheets of γ-Ga_2O_3 cannot be obtained without the coexistence of large amounts of VO in the samples [73]. The γ-Ga_2O_3 nanostructures possess high VO concentrations and disorder compared with β-Ga_2O_3 [74]. The abundant unsaturated gallium atoms are active sites for catalytic activities [73] and recombination of charges [75].

Now we want to compare the present phenomenological model to the experimental data reported in Ref. [65], which demonstrated room-temperature ferromagnetism in oxygen-defective γ-Ga_2O_{3-x} ($0.42 < x < 0.60$) films with spinel-like cubic structure. According to experimental results, γ-Ga_2O_{3-x} films with stoichiometry close to optimized γ-$Ga_{24}O_{32}$ ($x = 0.42$ and 0.46) exhibit a persistent ferromagneticlike behavior even above 360 K, with magnetic moments between 0.10 and $0.14\mu_B$ per supercell after subtraction of

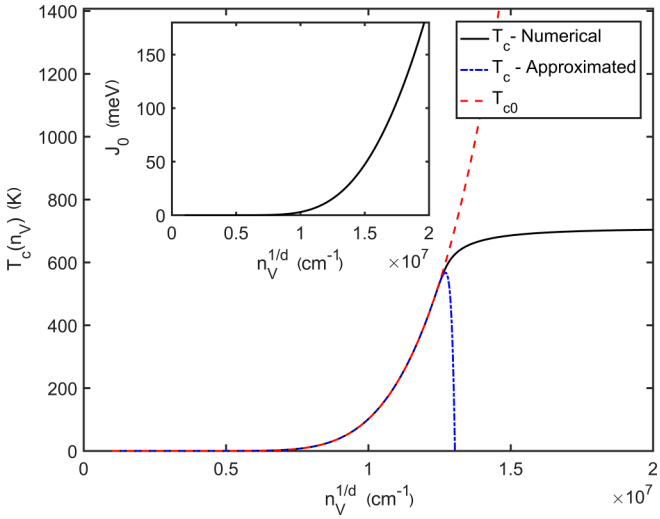

FIG. 7. The Curie temperature $T_c(n_V)$ is plotted against $n_V^{1/d}$ for the γ-Ga_2O_3 phase, using oxygen density $n = 4.42 \times 10^{22}$ cm^{-3}, dielectric constant $\epsilon_r = 5$, $E_0 = 0.9$ eV, vacancy charge $q = +2e$ and spin $S = 1/2$, coordination $z = 4$, and the effective parameter $\alpha^{-1} = 122$ pm. The inset displays the exchange parameter J_0 as a function of $n_V^{1/d}$.

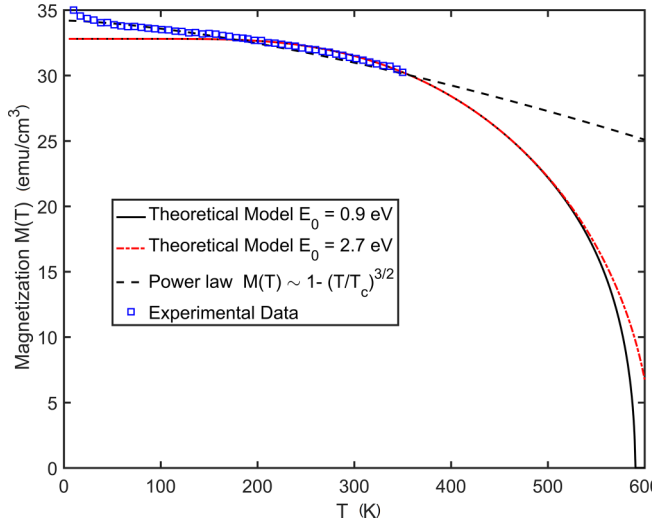

FIG. 8. Comparison between the theoretical model proposed here and the experimental data extracted from sample GA4 of Pichorim *et al.* [65]. The following parameters were used: effective spin $S = 1/2$, effective exchange energy $zJ_0 = 104$ meV, oxygen activation energy $E_0 = 0.9$ eV (black curve) and $E_0 = 2.7$ eV (red curve), $d = 3$, and $n = 5.8 \times 10^{22}$ cm^{-3}.

paramagnetic moment contributions from sapphire substrates. The optimized supercell has a lattice parameter $a = 0.8979$ nm, which implies an oxygen density $n = 4.42 \times 10^{22}$ cm^{-3} and a vacancy density in the range of $n_V = 2 \times 10^{21} - 5 \times 10^{21}$ cm^{-3}.

The film thickness was determined to be ∼30 nm, making the dimensionality more close to $d = 3$. The dielectric constant of the γ-Ga_2O_3 phase is $\epsilon_r \approx 5$, and the Ga atom has a covalent radius ∼122 pm, which is taken to be α^{-1}. The vacancy charge is taken to be again $q = +2e$, with effective spin $S = 1/2$. The coordination number z is between 4 and 8. We will adopt $z = 6$. The oxygen density in the γ phase is $n \approx 4.42 \times 10^{22}$ cm^{-3} for $d = 3$. The activation energy for oxygen diffusion E_0 is in the range $0.9 - 2.7$ eV. Figure 7 displays the behavior of the Curie temperature for the γ-Ga_2O_3 phase as a function of the vacancy concentration $n_V^{1/d}$ for $E_0 = 0.9$ eV. A maximum attainable T_c is around 700 K, which is reached at $n_V^{1/3} \approx 1.35 \times 10^7$ cm^{-1}.

Figure 8 shows the fitting of the experimental data for one of the γ-Ga_2O_{3-x} films reported in Ref. [65], having $x = 0.42$, using the model proposed here. The estimated number of vacancies is $n_V^{1/3} \approx 1.27 \times 10^7$ cm^{-1}, which implies $J_0 \approx 17.5$ meV. This way the parameters are the following: effective spin $S = 1/2$, effective exchange energy $zJ_0 = 105$ meV, two distinct values for the oxygen activation energy, $E_0 = 0.9$ eV and $E_0 = 2.7$ eV, $n = 4.42 \times 10^{22}$ cm^{-3}, $d = 3$. A power law of the form $M(T) = M_S[1 - (T/T_c)^{3/2}]$ is also displayed for the sake of comparison, with an effective $T_c \approx 1450$ K for the best fitting. The ratio between the measured value of $M_s \sim 33$ emu/cm^{-3} and the estimated value of vacancies n_V yields an effective magnetic moment $\mu_{eff} \approx 1.77\mu_B$.

It is also reported in Ref. [65] that the saturation magnetization is reduced with the increase in sample oxygen deficiency. For instance, the highest saturation was obtained by the sample with $x = 0.42$ and the lowest saturation for the sample with $x = 0.6$. This way the experimental data would seem to contradict the model put forward here. The authors of Ref. [65] attributed the reduction in saturation magnetization with increasing sample oxygen to the conflicting superposition of extended magnetic couplings. Indeed, there are two relevant aspects to be mentioned here: (i) the influence of structural disorder that is more pronounced in samples with greater oxygen deficiency (described in Ref. [76]), and (ii) the noncollinear ordering of magnetization (discussed in Ref. [65]) that certainly plays an important role in the magnetic behavior of these samples, but are beyond the scope of this model.

It is worth mentioning that the available experimental values were taken at temperatures below the transition temperature to a paramagnetic state. Therefore the critical behavior can only be estimated, based on the fact that in Ga_2O_3 the γ phase has a transition to a β phase at ∼650 K. In the present model, if one is confident in the estimated value for J_0, the main parameter regulating the critical temperature is the activation energy E_0. As previously mentioned, the current literature puts the lower limit to 0.7 eV and an upper limit at around 2.7 eV.

C. MoS_2

Pristine molybdenum disulfide (MoS_2) nanosheets have hexagonal crystal structure with trigonal prismatic (2H) and octahedral (1T) unit-cell structures. Among possible Mo and S vacancies, the defect composed of one Mo and two S vacancies (V^*) in the few-layered MoS_2 films is the most strong candidate to exhibit magnetization behavior. The defect V^* concentration increased from 0.0% to 6.3% using γ-ray

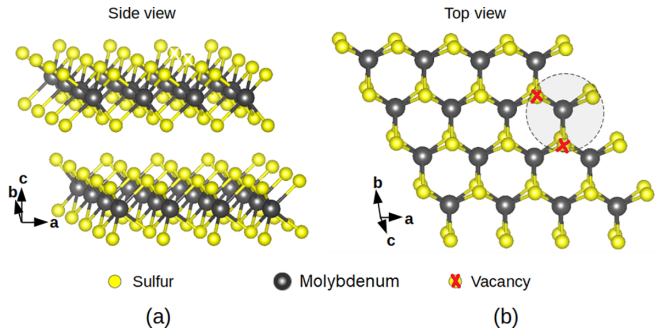

FIG. 9. Molybdenum disulfide (MoS_2) in the stable hexagonal phase (2H). Side view showing (a) two MoS_2 monolayers consisting of three S-Mo-S atomic layers that are held together by weak van der Waals interactions. (b) Top view of a MoS_2 monolayer showing Mo-S bonds with hexagonal symmetry. Isolated sulfur vacancies tend to form divacancy complexes (dashed circular area) and migrate over the lattice.

irradiation gives magnetic moments from $1.50\mu_B$ to $4.77\mu_B$ [20].

Basically, sulfur vacancies (VS) with trapped electrons interact with the Mo $4d$ spin-1/2 magnetic moments, resulting in the formation of bound magnetic polarons (BMPs), and when there is a certain distribution of sufficient defects within the samples, a significant overlapping of the BMPs gives rise to a robust ferromagnetism. Both vacancies have been shown to migrate to adjacent sites. Migrations can occur when an electron scatters off a Mo atom that neighbors a vacancy. If the scattered electron imparts enough momentum to the Mo in the direction of the vacancy, the Mo atom tends to migrate into the vacant site, leaving behind a new vacancy. Thus the term migration refers to the migration of both sulfur vacancies, divacancy clusters, and trefoil defect centers that form V^* clusters [21], as shown in Fig. 9. These V^* complexes have relatively high formation energy. Average activation energy for migration depends on the number of nearest-neighbor vacancies, and even at room temperature, S vacancies can migrate [21].

The present phenomenological model also can be applied to describe the magnetization of defective MoS_2 films. For the sake of comparison, experimental data was extracted from Ref. [15]. The density of sulfur atoms in MoS_2 is estimated to be $n = 3.6 \times 10^{22}$ cm^{-3}, while for a ~2-nm film we assume $n \approx 7.2 \times 10^{15}$ cm^2. For the films reported in Ref. [15], we have estimated a sulfur vacancy density of $n_V^{1/2} \approx 1.075 \times 10^7$ cm^{-1}, which yields $J_0 \approx 11.3$ meV for a typical dielectric constant $\epsilon_r = 5$ and Mo covalent radius $\alpha^{-1} = 138$ pm, while the sulfur mass is $m = 32$ Da. The behavior of the Curie temperature as a function of the sulfur vacancy concentration $n_V^{1/d}$ for MoS_2 is displayed in Fig. 10. The value of $E_0 = 0.42$ eV was adopted to obtain the fitting. As can be seen from Fig. 10, a maximum attainable T_c is ~540 K, which is reached at $n_V^{1/3} \approx 1.5 \times 10^7$ cm^{-1}.

Figure 11 illustrates the fitting using effective spin $S = 2$ in this case, exchange energy $zJ_0 = 34$ meV, and activation energy $E_0 = 0.42$ eV, which makes it possible for the sulfur atoms to migrate even at room temperature, and $n = 7.2 \times$

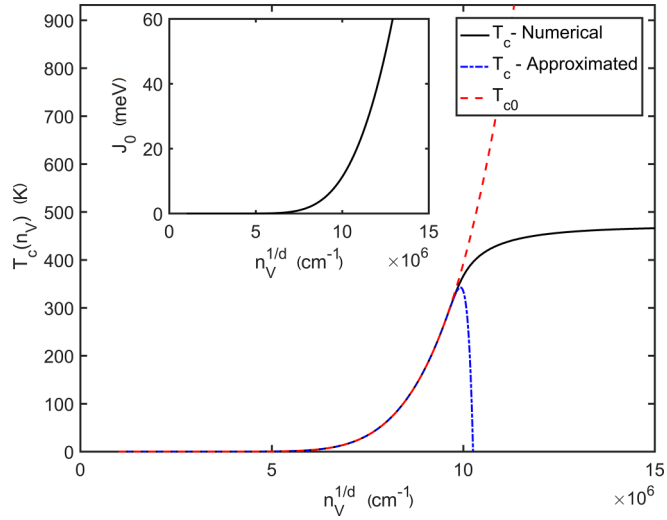

FIG. 10. The Curie temperature $T_c(n_V)$ is plotted vs $n_V^{1/d}$ for MoS_2 using sulfur density $n = 3.6 \times 10^{22}$ cm^{-3}, dielectric constant $\epsilon_r = 5$, $E_0 = 0.42$ eV, vacancy charge $q = +2e$ and spin $S = 2$, sulfur mass $m = 32$ Da, coordination $z = 3$, and effective parameter $\alpha^{-1} = 138$ pm. The inset displays the exchange parameter J_0 as a function of $n_V^{1/d}$.

10^{15} cm^{-2} in $d = 2$. As can be seen, the model is in good agreement with experimental data.

The saturation magnetization is estimated to be $M_s = \mu_{eff} n_V \approx 5$ emu/cm^3, assuming $\mu_{eff} = 0.5\mu_B$. It is in good agreement with the reported value of 1 emu/g [15], if we consider the MoS_2 density to be 5.06 g/cm^3.

IV. CONCLUSION

The model proposed in this work was applied to oxygen-deficient TiO_2 and Ga_2O_3 nanostructures that exhibit fer-

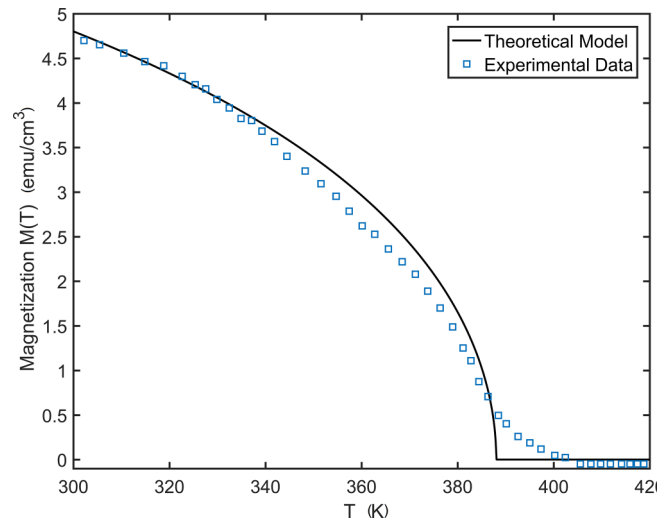

FIG. 11. Comparison between the theoretical model proposed here and the experimental data extracted from Liang Cai *et al.* [15] for defective MoS_2 films. The following parameters were used: effective spin $S = 2$, effective exchange energy $zJ_0 = 34$ meV, oxygen activation energy $E_0 = 0.42$ eV, $d = 2$, and $n = 7 \times 10^{15}$ cm^{-2}.

romagneticlike behavior at room temperature. The oxygen vacancy diffusion and oxygen migration mechanisms used in our model corroborate the results obtained in several experiments and DFT theoretical calculations gathered in the literature. The nonlocalized magnetism resulting from charge and spin migration used here is in agreement with the DFT calculations found in the literature predicting significant interstitial magnetic moments that favor the stabilization of the magnetic order. In the lamellar system of MoS_2, model validation is faced with two limiting situations. The first is the prediction of high values of migration energy barriers at room temperature and the second is the mobility of an extended defect consisting of a complex of two isolated sulfur vacancies. Despite these experimental conditions, the proposed model presents very reasonable results for the magnetization behavior as a function of temperature. As a final remark, the presented discussion is based on the assumption that atoms and vacancies can acquire a new lattice site during jump migration driven by thermodynamic forces of thermal and diffusional nature. This restriction is not essential, as two, three, or more atoms can be cooperatively involved to jump to new sites, provided that the topology of the contours and configuration space of energy barriers favor this.

ACKNOWLEDGMENTS

The authors acknowledge support of the INCT of Spintronics and Advanced Magnetic Nanostructures (INCT-SpinNanoMag), CNPq 406836/2022-1, and partial financial support from the CNPq (404023/2021- 5) and CAPES agencies. They also thank the anonymous referees for useful contributions and discussions, which made possible a significant improvement of this paper.

All authors contributed equally to this work.

All authors reviewed the manuscript.

[1] R. M. T. Araujo, J. Zarpellon, and D. H. Mosca, Unveiling ferromagnetism and antiferromagnetism in two dimensions at room temperature, J. Phys. D: Appl. Phys. **55**, 283003 (2022).

[2] G. Z. Magda, X. Jin, I. Hagymási, P. Vancsó, Z. Osváth, P. Nemes-Incze, C. Hwang, L. P. Biró, and L. Tapasztó, Room-temperature magnetic order on zigzag edges of narrow graphene nanoribbons, Nature (London) **514**, 608 (2014).

[3] S. Li, G. Ji, and L. Lü, Magnetic carbon nanofoams, J. Nanosci. Nanotech. **9**, 1133 (2009).

[4] W. Orellana and P. Fuentealba, Structural, electronic and magnetic properties of vacancies in single-walled carbon nanotubes, Surf. Sci. **600**, 4305 (2006).

[5] K. W. Lee, H. Kweon, and C. E. Lee, Field-induced transition from room-temperature ferromagnetism to diamagnetism in proton-irradiated fullerene, Adv. Mater. **25**, 5663 (2013).

[6] H. Ren and G. Xiang, Strain-modulated magnetism in MoS2, Nanomaterials **12**, 1929 (2022).

[7] H. Wu, W. Zhang, L. Yang, J. Wang, J. Li, L. Li, Y. Gao, L. Zhang, J. Du, H. Shu, and H. Chan, Strong intrinsic room-temperature ferromagnetism in freestanding non-van der Waals ultrathin 2D crystals, Nat. Commun. **12**, 5688 (2021).

[8] P. Esquinazi, W. Hergert, D. Spemann, A. Setzer, and A. Ernst, Defect-induced magnetism in solids, IEEE Trans. Magn. **49**, 4668 (2013).

[9] A. Sundaresan, R. Bhargavi, N. Rangarajan, U. Siddesh, and C. N. R. Rao, Ferromagnetism as a universal feature of nanoparticles of the otherwise nonmagnetic oxides, Phys. Rev. B **74**, 161306(R) (2006).

[10] S. B. Ogale, Dilute doping, defects, and ferromagnetism in metal oxide systems, Adv. Mater. **22**, 3125 (2010).

[11] K. Ackland and J. M. D. Coey, Room temperature magnetism in CeO_2 - A review, Phys. Rep. **746**, 1 (2018).

[12] X. Wei, R. Skomski, B. Balamurugan, Z. G. Sun, S. Ducharme, and D. J. Sellmyer, Magnetism of TiO and TiO_2 nanoclusters, J. Appl. Phys. **105**, 07C517 (2009).

[13] S. D. Yoon, Y. Chen, A. Yang, T. L. Goodrich, X. Zuo, D. A. Arena, K. Ziemer, C. Vittoria, and V. G. Harris, Oxygen defect induced magnetism to 880 K in semiconducting anatase $TiO_{2-\delta}$ films, J. Phys.: Condens. Matter **18**, L355 (2006).

[14] A. Hassini, J. Sakai, J. S. Lopez, and N. H. Hong, Magnetism in spin-coated pristine TiO_2 thin films, Phys. Lett. A **372**, 3299 (2008).

[15] L. Cai, J. He, Q. Liu, T. Yao, L. Chen, W. Yan, F. Hu, Y. Jiang, Y. Zhao, T. Hu, Z. Sun, and S. Wei, Vacancy-induced ferromagnetism of MoS_2 nanosheets, J. Am. Chem. Soc. **137**, 2622 (2015).

[16] M. Stiller, J. Barzola-Quiquia, P. Esquinazi, D. Spemann, J. Meijer, M. Lorenz, and M. Grundmann, Strong out-of-lane magnetic anisotropy in ion irradiated anatase TiO_2 thin films, AIP Adv. **6**, 125009 (2016).

[17] B. Bharati, N. C. Mishra, and C. Rath, Effect of 500 keV Ar2+ ion irradiation on structural and magnetic properties of TiO_2 thin films annealed at 900°C, Appl. Surf. Sci. **455**, 717 (2018).

[18] H. Liu, G. P. Li, Q. L. Lin, D. J. E, X. D. Gao, X. B. Wei, X. D. Pan, S. X. Zhang, J. J. Ding, and W. Lan, Oxygen vacancy-induced room temperature ferromagnetism in rutile TiO_2, J. Supercond. Nov. Magn. **32**, 3557 (2019).

[19] V. Fernandes, I. L. Graff, J. Varalda, L. Amaral, P. F. P. Fichtner, D. Demaille, Y. Zheng, W. H. Schreiner, and D. H. Mosca, Valence evaluation of cerium in nanocrystalline CeO_2 films electrodeposited on Si substrates, J. Electrochem. Soc. **159**, K27 (2011).

[20] A. K. Anbalagan, F.-C. Hu, W. K. Chan, A. C. Gandhi, S. Gupta, M. Chaudhary, K.-W. Chuang, A. K. Ramesh, T. Billo, A. Sabbah, C.-Y. Chiang, Y.-C. Tseng, Y.-L. Chueh, S. Y. Wu, N.-H. Tai, H.-Y. T. Chen, and C.-H. Lee, Gamma-ray irradiation induced ultrahigh room-temperature ferromagnetism in MoS_2 sputtered few-layered thin films, ACS Nano **17**, 6555 (2023).

[21] A. Yoshimura, M. Lamparski, N. Kharche, and V. Meunier, First-principles simulation of local response in transition metal dichalcogenides under electron irradiation, Nanoscale **10**, 2388 (2018).

[22] P. Castro-Fernández, D. Mance, C. Liu, P. M. Abdala, E. Willinger, A. A. Rossinelli, A. I. Serykh, E. A. Pidko, C. Copéret, A. Fedorov, and C. R. Müller, Bulk and surface transformations of $Ga_2O_3MoS_2$ nanoparticle catalysts for propane

dehydrogenation induced by a H_2 treatment, J. Catal. **408**, 155 (2022).

[23] Z.-K. Han, L. Zhang, M. Liu, M. V. Ganduglia-Pirovano, and Y. Gao, The structure of oxygen vacancies in the near-surface of reduced CeO_2 (111) under strain, Front. Chem. **7**, 436 (2019).

[24] S. Arapan, S. I. Simak, and N. V. Skorodumova, Volume-dependent electron localization in ceria, Phys. Rev. B **91**, 125108 (2015).

[25] T. Mayeshiba and D. Morgan, Strain effects on oxygen vacancy formation energy in perovskites, Solid State Ionics **311**, 105 (2017).

[26] Z. Zarhri, M. Houmad, Y. Ziat, O. El Rhazouani, A. Slassi, A. Benyoussef, and A. El Kenz, Ab-initio study of magnetism behavior in TiO_2 semiconductor with structural defects, J. Magn. Magn. Mater. **406**, 212 (2016).

[27] J. M. D. Coey, d^0 ferromagnetism, Solid State Sci. **7**, 660 (2005).

[28] J. M. D. Coey, M. Venkatesan, and C. B. Fitzgerald, Donor impurity band exchange in dilute ferromagnetic oxides, Nat. Mater. **4**, 173 (2005).

[29] J. M. D. Coey, Dilute magnetic oxides, Curr. Opin. Solid State Mater. Sci. **10**, 83 (2006).

[30] J. M. D. Coey, A. P. Douvalis, C. B. Fitzgerald, and M. Venkatesan, Ferromagnetism in Fe-doped SnO_2 thin films, Appl. Phys. Lett. **84**, 1332 (2004).

[31] A. C. Durst, R. N. Bhatt, and P. A. Wolff, Bound magnetic polaron interactions in insulating doped diluted magnetic semiconductors, Phys. Rev. B **65**, 235205 (2002).

[32] J. Varalda, C. A. Dartora, P. C. de Camargo, A. J. A. de Oliveira, and D. H. Mosca, Oxygen diffusion and vacancy migration thermally-activated govern high-temperature magnetism in ceria, Sci. Rep. **9**, 4708 (2019).

[33] A. Altland and B. Simmons, *Condensed Matter Field Theory*, 2nd ed. (Cambridge University Press, Cambridge, England, 2010).

[34] D. A. H. Hanaor and C. C. Sorrell, Review of the anatase to rutile phase transformation, J. Mater. Sci. **46**, 855 (2011).

[35] S. K. Kim, W.-D. Kim, K.-M. Kim, C. S. Hwang, and J. Jeong, High dielectric constant TiO_2 thin films on a Ru electrode grown at 250°C by atomic-layer deposition, Appl. Phys. Lett. **85**, 4112 (2004).

[36] M. Kadoshima, M. Hiratani, Y. Shimamoto, K. Torii, H. Miki, S. Kimura, and T. Nabatame, Rutile-type TiO_2 thin film for high-κ gate insulator, Thin Solid Films **424**, 224 (2003).

[37] M. D. Stamate, On the dielectric properties of dc magnetron TiO_2 thin films, Appl. Surf. Sci. **218**, 318 (2003).

[38] T. B. Gruenwald and G. Gordon, Oxygen diffusion in single crystals of titanium dioxide, J. Inorg. Nucl. Chem. **33**, 1151 (1971).

[39] A. N. Bagshaw and B. G. Hyde, Oxygen tracer diffusion in the Magnéli phases Ti_nO_{2n-1}, J. Phys. Chem. Solids **37**, 835 (1976).

[40] M. Arita, M. Hosoya, M. Kobayashi, and M. Someno, Depth profile measurement by secondary ion mass spectrometry for determining the tracer diffusivity of oxygen in rutile, J. Am. Ceram. Soc. **62**, 443 (1979).

[41] F. Millot and C. Picard, Oxygen self-diffusion in non-stoichiometric rutile TiO_2 at high temperature, Solid State Ionics **28-30**, 1344 (1988).

[42] X. Cui, B. Wang, Z. Wang, T. Huang, Y. Zhao, J. Yang, and J. G. Hou, Formation and diffusion of oxygen-vacancy pairs on TiO_2, J. Chem. Phys. **129**, 044703 (2008).

[43] X. Chen and S. S. Mao, Titanium dioxide nanomaterials: Synthesis, properties, modifications, and applications, Chem. Rev. **107**, 2891 (2007).

[44] X. Pan, M.-Q. Yang, X. Fu, N. Zhanga, and Y.-J. Xu, Defective TiO_2 with oxygen vacancies: Synthesis, properties and photocatalytic applications, Nanoscale **5**, 3601 (2013).

[45] K. Szot, M. Rogala, W. Speier, Z. Klusek, A. Besmehn, and R. Waser, TiO_2 – A prototypical memristive material, Nanotechnology **22**, 254001 (2011).

[46] K. Zakrzewska, Gas sensing mechanism of TiO_2-based thin films, Vacuum **74**, 335 (2004).

[47] K. M. Pangan-Okimoto, P. Gorai, A. G. Hollister, and E. G. Seebauer, Model for oxygen interstitial injection from the rutile TiO_2(110) surface into the bulk, J. Phys. Chem. C **119**, 9955 (2015).

[48] E. Cho, S. Han, H.-S. Ahn, K.-R. Lee, S. K. Kim, and C. S. Hwang, First-principles study of point defects in rutile TiO_{2-x}, Phys. Rev. B **73**, 193202 (2006).

[49] P. M. Kowalski, M. F. Camellone, N. N. Nair, B. Meyer, and D. Marx, Charge localization dynamics induced by oxygen vacancies on the TiO_2 (110) surface, Phys. Rev. Lett. **105**, 146405 (2010).

[50] H. H. Pham and L-W. Wang, Oxygen vacancy and hole conduction in amorphous TiO_2, Phys. Chem. Chem. Phys. **17**, 541 (2015).

[51] Y. Shi, H. Sun, M. C. Nguyen, C. Wang, K. Ho, W. A. Saidid, and J. Zhao, Structures of defects on anatase TiO_2 (001) surfaces, Nanoscale **9**, 11553 (2017).

[52] M. Reticcioli, M. Setvin, M. Schmid, U. Diebold, and C. Franchini, Formation and dynamics of small polarons on the rutile TiO_2 (110) surface, Phys. Rev. B **98**, 045306 (2018).

[53] G. Thorwarth, S. Mändel, and B. Rauschenbach, Rutile formation and oxygen diffusion in oxygen PIII-treated titanium, Surf. Coat. Technol. **136**, 236 (2001).

[54] G. G. Marmitt, S. K. Nandi, D. K. Venkatachalam, R. G. Elliman, M. Vos, and P. L. Grande, Oxygen diffusion in TiO_2 films studied by electron and ion Rutherford backscattering, Thin Solid Films **629**, 97 (2017).

[55] A. Yildiz, S. B. Lesesivdin, M. Kasap, and D. Mardare, Electrical properties of TiO_2 thin films, J. Non-Cryst. Solids **354**, 4944 (2008).

[56] V. Z. C. Paes, D. H. Mosca, A. J. A. de Oliveira, and J. Varalda, Non-conventional ferromagnetism and high bias magnetoresistance in TiO_{2-x}: A simple phenomenological approach, J. Magn. Magn. Mater. **497**, 166068 (2020).

[57] K. Jug, N. N. Nair, and T. Bredow, Molecular dynamics investigation of oxygen vacancy diffusion in rutile, Phys. Chem. Chem. Phys. **7**, 2616 (2005).

[58] Y. Alivov, T. Grant, C. Capan, W. Iwamoto, P. G. Pagliuso, and S. Molloi, Origin of magnetism in undoped TiO_2 nanotubes, Nanotechnology **24**, 275704 (2013).

[59] B. Santara, P. K. Giri, K. Imakita, and M. Fujii, Evidence of oxygen vacancy induced room temperature ferromagnetism in solvothermally synthesized undoped TiO_2 nanoribbons, Nanoscale **5**, 5476 (2013).

[60] S. D. Yoon, Y. C. A. Yang, T. L. Goodrich, X. Zuo, K. Ziemer, C. Vittoria, and V. G. Harris, Magnetic semiconducting anatase

$TiO_{2-\delta}$ grown on (100) $LaAlO_3$ having magnetic order up to 880K, J. Magn. Magn. Mater. **309**, 171 (2007).

[61] H. Kawazoe and K. Ueda, Transparent conducting oxides based on the spinel structure, J. Am. Ceram. Soc **82**, 3330 (1999).

[62] H. Wang, R. P. Liu, Y. T. Li, X. J. Lü, Q. Wang, S. Q. Zhao, K. J. Yuan, Z. M. Cui, X. Li, S. Xin, R. Zhang, M. Lei, and Z. Q. Lin, Durable and efficient hollow porous oxide spinel microspheres for oxygen reduction, Joule **2**, 337 (2018).

[63] Y. Huang, A. Gao, D. Guo, X. Lu, X. Zhang, Y. Huang, J. Yu, S. Li, P. Li, and W. Tang, Fe doping-stabilized γ-Ga_2O_3 thin films with a high room temperature saturation magnetic moment, J. Mater. Chem. C **8**, 536 (2020).

[64] M. Zinkevich, F. M. Morales, H. Nitsche, M. Ahrens, M. Rühle, and F. Aldinger, Microstructural and thermodynamic study of γ-Ga_2O_3, Z. Metallkd. **95**, 756 (2004).

[65] A. Pichorim, I. T. Neckel, A. J. A. de Oliveira, J. Varalda, and D. H. Mosca, Room temperature ferromagnetism in oxygen-deficient gallium oxide films with cubic spinel structure, Mater. Chem. Phys. **287**, 126320 (2022).

[66] A. Kyrtsos, M. Matsubara, and E. Bellotti, Migration mechanisms and diffusion barriers of vacancies in Ga_2O_3, Phys. Rev. B **95**, 245202 (2017).

[67] L. Dong, R. Jia, B. Xin, and Y. Zhang, Effects of post-annealing temperature and oxygen concentration during sputtering on the structural and optical properties of β-Ga_2O_3 films, J. Vac. Sci. Technol. A **34**, 060602 (2016).

[68] A. Usseinov, Z. Koishybayeva, A. Platonenko, V. Pankratov, Y. Suchikova, A. Akilbekov, M. Zdorovets, J. Purans, and A. I. Popov, Vacancy defects in Ga_2O_3: First-principles calculations of electronic structure, Materials **14**, 7384 (2021).

[69] L. Dong, R. Jia, B. Xin, B. Peng and Y. Zhang, Effects of oxygen vacancies on the structural and optical properties of β-Ga_2O_3, Sci. Rep. **7**, 40160 (2017).

[70] Y. Yang, J. Zhang, S. Hu, Y. Wu, J. Zhang, W. Ren, and S. Cao, First-principles study of Ga-vacancy induced magnetism in β-Ga_2O_3, Phys. Chem. Chem. Phys. **19**, 28928 (2017).

[71] M. D. McCluskey, Point defects in Ga_2O_3, J. Appl. Phys. **127**, 101101 (2020).

[72] Y. K. Frodason, J. B. Varley, K. Magnus, H. J. L. Vines, and C. G. Van de Walle, Migration of Ga vacancies and interstitials in β-Ga_2O_3, Phys. Rev. B **107**, 024109 (2023).

[73] X. Zhang, Z. Zhang, J. Lin, D. Liu, and X. Wan, Oxygen vacancy modulation of two-dimensional γ-Ga_2O_3 nanosheets as efficient catalysts for photocatalytic hydrogen evolution, Nanoscale **10**, 21509 (2018).

[74] X. Zhang, H. Huang, Y. Zhang, D. Liu, N. Tong, J. Lin, L. Chen, Z. Zhang, and X. Wang, Phase transition of two-dimensional β-Ga_2O_3 nanosheets from ultrathin γ-Ga_2O_3 nanosheets and their photocatalytic hydrogen evolution activities, ACS Omega **3**, 14469 (2018).

[75] T. Wang and P. V. Radovanovi, In situ enhancement of the blue photoluminescence of colloidal Ga_2O_3 nanocrystals by promotion of defect formation in reducing conditions, Chem. Commun. **47**, 7161 (2011).

[76] A. Pichorim, D. S. Costa, I. T. Neckel, and D. H. Mosca, Non-stoichiometric gallium oxide with cubic structure directly integrated to C-Cut sapphire, Mater. Sci. Semicond. Process. **139**, 106349 (2022).